Manipulation of Nanodroplets via a Nonuniform Focused Acoustic Vortex

Shifang Guo,[1,*] Xuyan Guo,[1] Xin Wang,[1] Xuan Du,[1] Pengying Wu,[1] Ayache Bouakaz,[1,2] and Mingxi Wan[1,†]

[1] *The Key Laboratory of Biomedical Information Engineering of Ministry of Education, Department of Biomedical Engineering, School of Life Science and Technology, Xi'an Jiaotong University, Xi'an 710049, People's Republic of China*

[2] *UMR 1253, iBrain, Université de Tours, Inserm, Tours, France*

(Received 15 October 2019; revised manuscript received 4 February 2020; accepted 11 February 2020; published 3 March 2020)

Techniques for the manipulation of nanodroplets are central to many miniaturized systems in chemical and biological research and applications. In this study, we demonstrate that the dispersed nanodroplets composed of perfluorocarbon can be manipulated to form a micron-sized elliptical aggregation via a nonuniform focused acoustic vortex, and the aggregation location can be further flexibly regulated. In addition, it is unveiled theoretically and experimentally that the fundamental mechanism for the elliptical aggregation is the nonuniform distribution of the pressure, which makes the acoustic radiation forces acting on the dispersed nanodroplets converge at a certain point. Moreover, the required acoustic droplet vaporization threshold for the nanodroplets is significantly lowered, while the generated microbubbles remain similar in size after aggregation. The findings of this study provide an alternative field of opportunities for targeted drug delivery and imaging using nanodroplet emulsions.

DOI: 10.1103/PhysRevApplied.13.034009

I. INTRODUCTION

The development of stimulus-sensitive nanoparticulate pharmaceutical drug delivery systems to enhance the *in vivo* effectiveness of drugs has been an active area of research in recent decades [1]. Owing to the impressive progress in materials science and pharmaceutics, a broad range of nanocarriers with diverse sizes, architectures, and surface properties have been designed [2]. Among them, nanodroplets composed of perfluorocarbon have been shown to represent a system that is potentially efficient enough to deliver drugs in a spatiotemporally controllable manner [3]. The nanodroplets remain in a liquid state at body temperature and have a long residual time (up to several days). Furthermore, they can be vaporized locally when triggered by ultrasonic pulses, commonly known as acoustic droplet vaporization (ADV), which can be easily and accurately detected by ultrasound imaging [4,5]. Moreover, the nanodroplets are considered to be an ideal system for targeted drug delivery because they can be easily combined with other materials, and have enhanced vascular permeability due to their nanoscale size [2,5]. Even more importantly, the interaction of vaporized microbubbles with ultrasound can facilitate drug uptake into cells *in situ* by enhanced drug extravasation and transcellular permeability due to microstreaming and shear stress [6,7]. Manipulating nanodroplets in the target areas may yield many valuable benefits, such as increasing the nanodroplet concentration in the therapeutic site, and reducing the distance between the nanodroplets and the vessel wall. Various manipulation techniques for particles have been developed, such as optical tweezers, atomic force microscopy, and micropipette aspiration. Among them, acoustic tweezers have been shown to have great potential for *in vivo* applications because they can penetrate deeply, cause less tissue damage, and make no contact with the target [8,9].

It is well known that acoustic waves can exert radiation forces on particles [10], and can form acoustic traps at points where the forces converge, thus permitting the capture of particles [11–13]. In 1991, Wu generated a stable force potential well in ultrasonic standing waves (USWs) by applying two opposing transducers, and introduced the term of acoustic tweezers [14]. To date, it has been shown that various objects of different sizes and materials such as cells, compounds, or living things can be manipulated by USWs [15,16]. Our previous study demonstrated that dispersed nanodroplets can be aggregated in USWs to form clusters with diameters of tens of microns [8]. However, USWs require the targets to be enclosed with ultrasonic elements and have repeated patterns that can accidentally trap other particles or generate undesired secondary

*sfguobme@mail.xjtu.edu.cn
†mxwan@mail.xjtu.edu.cn

maxima, leading to limited maneuverability and potential risks [17,18].

Acoustic vortices provide a single-beam approach to manipulate particles [19,20], making it highly preferable and more practical compared to USWs [18]. The axial null in acoustic vortices can act as a collection of nodal points for the capture of particles [18,21]. The momentum transfer from acoustic vortices to matter has been studied theoretically [22,23] and experimentally [19,21,24–26]. Moreover, the propagation of acoustic vortices through weakly heterogeneous or inhomogeneous media has also been studied [27,28]. However, all the previously mentioned studies focus on the manipulation of solid particles or gaseous bubbles. Research on the manipulation of perfluorocarbon nanodroplets, which have different acoustic characteristics from the other two kinds of particles [29,30], has not yet been reported. Moreover, the aforementioned studies have been carried out in air or free-field solutions. Therefore, there is currently a lack of research addressing the potential applications of acoustic vortices on intravascular particles. Furthermore, no reported studies have described the properties of a nonuniform focused acoustic vortex, which may have unique advantages compared to the uniform acoustic vortex in certain contexts.

In this study, we propose a versatile approach to manipulate the intravascular perfluorocarbon nanodroplets using a nonuniform focused acoustic vortex. The process of nanodroplet aggregation is observed in real time using high-speed photomicrography, and its mechanism is explored theoretically and experimentally. Furthermore, the effects of nanodroplet aggregation on the ADV threshold and initial radius distribution of the generated microbubbles are explored.

II. MATERIALS AND METHODS

A. Transparent blood-vessel phantom preparation

An optically transparent phantom with a wall-less vessel 6 mm in diameter, exhibiting similar acoustic characteristics as soft tissues, is employed to mimic a vessel in soft tissues [31,32]. The preparation of the transparent blood-vessel phantom is as follows: First, a 40% (w/v) acrylamide solution is prepared and then evenly mixed with 1.1% (w/v) N,N'-methylene bis-acrylamide and deionized water. Second, the gel-mix liquid is poured into a rectangular box (length × width × height = 16 cm × 4 cm × 5.5 cm), whose center is traversed by a cylinder rod with a diameter of 6 mm. Third, after the liquid mixture has fully solidified, the cylinder rod is carefully removed to form a wall-less vessel with an approximate diameter of 6 mm. The density, ultrasound speed, and attenuation coefficient for the phantom at 1 MHz are equal to 1.003 ± 0.001 g/cm^3, 1512.2 ± 3.0 m/s, and 0.2 ± 0.01 dB/cm, respectively. The storage modulus of the phantom is in the range 2–8 kPa, and the loss modulus of the phantom is in the range 0.4–0.9 kPa [32].

B. Nanodroplet preparation and characterization

Nanodroplet emulsions are prepared by combining 5% (v/v) perfluorohexane (PFH), 0.8% (v/v) negatively charged fluorinated surfactant Capstone® FS-63 (DuPont, USA), and degassed deionized water [33]. The mixed samples are emulsified using an ultrasonic liquid processor (VC 705, Sonic & Materials, Newton, USA) at an 80% duty cycle for 60 s. The perfluorohexane liquid is clear and colorless, and the manufactured nanodroplets are light milky white. The size distribution of the nanodroplets is measured by dynamic light scattering using a Zetasizer nanosizing system. The concentration of the nanodroplets under investigation can be estimated based on the nanodroplet size distribution and the perfluorohexane volume used for the emulsion. The total volume of the nanodroplets in the sample can be expressed as [34]

$$V_{\mathrm{PFH}} = N \int_0^\infty \frac{4}{3}\pi R_d^3 k(R_d) dR_d, \tag{1}$$

where V_{PFH} represents the total volume of the PFH used in the nanodroplet preparation process, N is the total number of nanodroplets, and $k(R_d)$ means the fraction of the nanodroplets with a radius of R_d in the emulsion. Rearranging the terms in (1) gives [34]

$$N = \frac{3V_{\mathrm{PFH}}}{4\pi} \Big/ \int_0^\infty R_d^{3k}(R_d) dR_d. \tag{2}$$

Then the total number of nanodroplets in the emulsion can be calculated from the overall PFH volume and the nanodroplet size distribution. Throughout the experiments, the nanodroplet emulsions are diluted by saline at a series of volume ratios (100, 200, and 400 times).

C. Experimental setup

An immersed, spherical ultrasound transducer (Chongqing Ronghai Ultrasonic Medical Engineering Research Center Inc., Chongqing, China) with a central frequency of $f_1 = 660$ kHz (hereinafter referred to as the acoustic vortex transducer) is used to generate the required nonuniform focused acoustic vortex throughout this study. The transducer had a diameter of 120 mm, a curvature radius of 120 mm, and a central circular hole with a radius of 25 mm. The axisymmetric active surface of the acoustic vortex transducer is equally divided into 16 sectors, as shown in Figs. 1(a) and 1(b). Each sector of the transducer is connected to an independent channel of a power amplification system. The amplification system is in turn fed by using 16 channels of a timing control system, which generate sinusoidal signals in continuous mode and ensure a

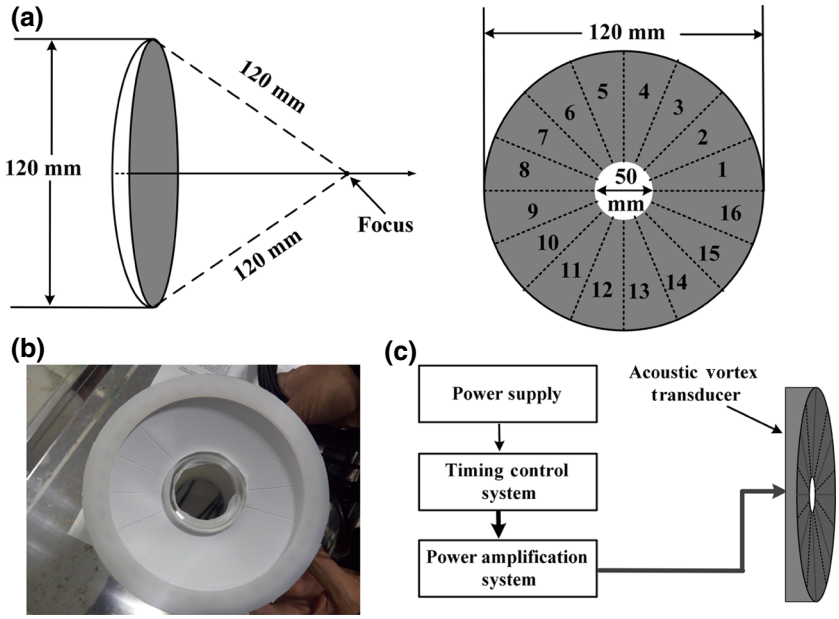

FIG. 1. (a) Schematic illustration and (b) photography of the acoustic vortex transducer; (c) diagram illustrating the generating system for the nonuniform focused acoustic vortex.

$(16 f_1)^{-1}$ time-delay increase between two adjacent channels, which is similar to the methods in Refs [19,22,25], as shown in Fig. 1(c). However, the power for each sector is set different in order to generate the required nonuniform acoustic vortex. A focused ultrasound transducer (diameter 28.575 mm, I8-0518-P, Olympus NDT Inc., Waltham, MA, USA) with a central frequency of 5 MHz, located vertically to the axis of the acoustic vortex transducer, is used as the cavitation transducer in this study. The cavitation transducer transmits a tone burst lasting 4 μs to initiate ADV before and after the aggregation in order to explore the changes in ADV threshold and the initial radius distribution of the generated microbubbles. A polycarbonate bracket is used to fix the blood-vessel phantom to a three-dimensional (3D) position controller, which is manually operated and located on one side of the water tank. The processes of nanodroplet aggregation, ADV, and the dissolution of the generated microbubbles are observed through a high-speed photography camera (Motion Pro Y3-S1, Integrated Design Tools Inc., MD, USA), as shown in Fig. 2(a).

D. Experimental protocol

The sequence of the experimental procedure is as follows. First, nanodroplet emulsions are pumped into the blood-vessel phantom, and then the pump is turned off. In this step, both the acoustic vortex and the cavitation transducers are turned off. Second, the acoustic vortex transducer is turned on to generate the required nonuniform focused acoustic vortex. In this step, the cavitation transducer is turned off. Under the action of the acoustic vortex, the dispersed nanodroplets are manipulated to form a micron-sized aggregation. Third, in order to explore the feasibility of adjusting the position of the nanodroplet aggregation relative to the blood-vessel phantom, the location of the phantom is adjusted by a 3D position controller while keeping the acoustic vortex transducer fixed. In this step, the acoustic vortex transducer is turned on, while the cavitation transducer is turned off. Forth, an ultrasonic pulse is transmitted by the cavitation transducer to induce the nanodroplet vaporization in order to explore the effects of aggregation on the ADV threshold and the initial radius distribution of the generated microbubbles. In this step, the cavitation transducer is turned on, and the acoustic vortex transducer is turned off at the same instant of time, thus eliminating the influence of the acoustic vortex on the ADV threshold determination.

E. Numerical calculations

In order to explore the mechanism underlying the nanodroplet aggregation, we simulate the nonuniform focused acoustic vortex generated by the system and calculate the acoustic radiation forces (ARFs) acting on particles. The former is based on an efficient field calculation formula from Rayleigh-Sommerfeld integral for calculating the pressure field generated by a spherical-section phased array, which is as follows [35]:

$$p = \frac{j\rho ck}{2\pi}\sum_{n=1}^{N} u_n \frac{F_n \Delta A}{R_n} e^{-(\alpha+jk)R_n} \sin c\frac{kx_{sn}\Delta w}{2R} \sin c\frac{ky_{sn}\Delta h}{2R} \tag{3}$$

where p represents the instantaneous acoustic pressure at a certain point in the calculated plane, j is the square root of -1, ρ and c are the density and sound speed in the surrounding medium, respectively, k is the wavenumber, α is the sound attenuation coefficient. N is the number of

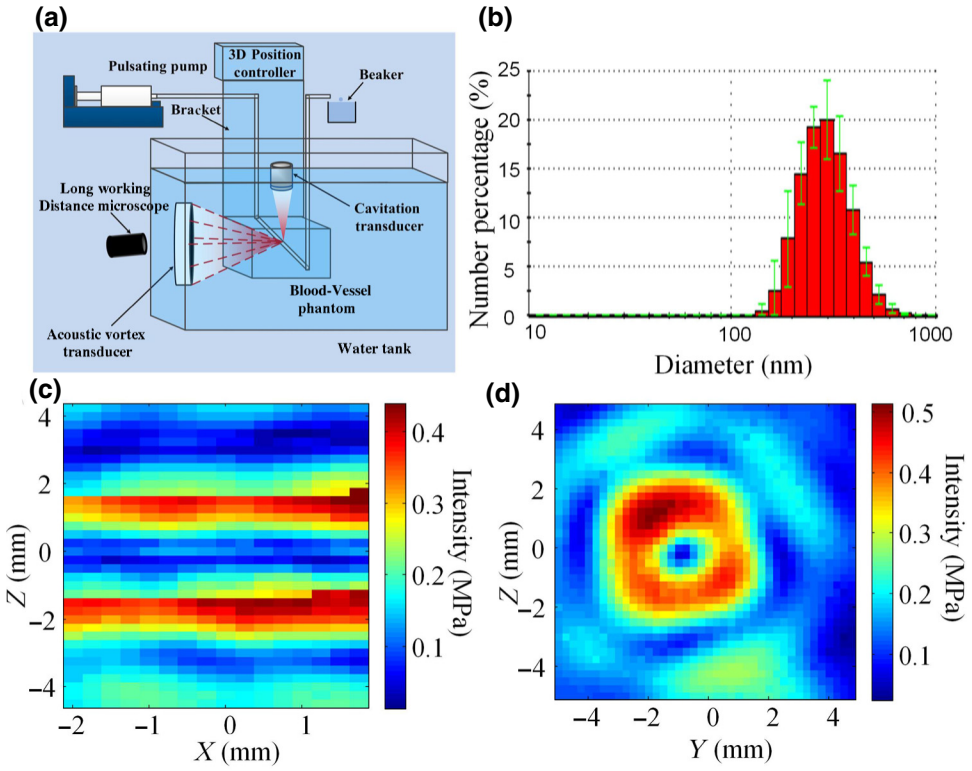

FIG. 2. (a) The experimental setup composed of two ultrasound transducers, a blood-vessel phantom, a microscope, a 3D position controller, and a pulsating pump. (b) Number distributions of a batch of perfluorohexane nanodroplets on the day of manufacturing. Color plot of the acoustic intensity in the (c) axial and (d) transverse plane of focus in the generated nonuniform focused acoustic vortex obtained by hydrophone scanning.

rectangular projections obtained by dividing the acoustic vortex transducer, and Δw, Δh, and ΔA are the width, height and area of each projection, respectively. u_n is the particle velocity of nth rectangular projection. R, F_n, R_n, x_{sn}, y_{sn} are several intermediate variables related to the location of the calculated point. More detailed information about the other parameters in Eq. (3) can be found in Refs. [35,36].

When a microbubble in liquid is subjected to an acoustic field, the oscillating pressure gradient can couple with the bubble oscillations to produce the translational force, i.e., the primary Bjerknes force, which takes the following form [37,38]:

$$F = -\langle V(t)\nabla P(r,t)\rangle, \tag{4}$$

where $V(t)$ represents the volume of a microbubble at time t and $P(r,t)$ is the acoustic pressure at position r at time t.

For nanodroplets, given the fact that their sizes are much smaller than the driving wavelength (approximately 2.3 mm) in the present study, the ARFs acting on them can be calculated based on the Rayleigh scattering regime. The potential energy of a nanodroplet can be expressed as

$$U = 2\pi r^3 \rho \left[\frac{\overline{p_{\text{in}}^2}}{3\rho^2 c^2} f_1 - \frac{\overline{v_{\text{in}}^2}}{2} f_2 \right]. \tag{5}$$

where r donates the particle radius, and p_{in} and v_{in} are the pressure and velocity within the incident wave at the location of the particle, and f_1 and f_2 are two constants related to the physical parameters of the particle and medium. More detailed information about the parameters in Eq. (5) can be found in Ref. [18]. Then the ARFs exerted on a nanodroplet can be obtained corresponding to the negative of the spatial gradient of the potential distribution.

The parameters in the numerical calculations are as follows. The radius of the acoustic vortex transducer's central circular hole is set to be consistent with that of the transducer used in the experiment, i.e., 25 mm. The surrounding medium is water at 25 °C, whose density and speed of sound are 1000 kg/m^3 and 1500 m/s, respectively [18]. The water is assumed to be an ideal fluid (i.e., no viscosity) to simplify the discussion. The density and speed of sound for the nanodroplets are 1680 kg/m^3 and 520 m/s, respectively [39].

III. RESULTS

The size distribution of the perfluorocarbon nanodroplets is shown in Fig. 2(b), with an average diameter of 408 ± 10.6 nm calculated by number percentage. Before the nanodroplet manipulation, a polyvinylidene fluoride (PVDF) hydrophone diameter of 1 mm is used to scan a grid of points defined near the focus with a step size of 0.25 mm to measure the acoustic pressure distribution in the generated acoustic vortex field. In the axial plane of the focus, the acoustic pressure distribution is characterized by low pressure in the middle and high pressure on both sides, as shown in Fig. 2(c), which is similar to the results

shown in Ref. [22]. In the transverse plane of the focus, the acoustic pressures form a "doughnut" pattern, but it is worth pointing out that they are not centrosymmetrical relative to the focus, as shown in Fig. 2(d). The pressures are stronger on the upper-left corner of the doughnut than in other parts, indicating the generation of a nonuniform focused acoustic vortex. The maximum value of the negative pressure in the doughnut is approximately 500 kPa. Our previous study demonstrated that the surfactant of the nanodroplets can avoid converging in an acoustic field that has a similar intensity to the generated acoustic vortex [8]. Therefore, it is believable that the nanodroplet size would not increase significantly after aggregation in the present study.

Figure 3(a) indicates that the dispersed nanodroplets are invisible in the optical images. This is due to the limited resolution of the optical images obtained in the study and the small volume ratio of nanodroplets in the intravascular solution (at most 0.05%). However, after the generation of the nonuniform focused acoustic vortex, the nanodroplets gradually aggregate into a cluster with a diameter of several hundred microns and the nanodroplet concentration in the aggregation area increases substantially, making the aggregation visible in the images. The aggregation is found to appear as an opaque elliptical area, and can only be identified after 30 s (see Video S1 in the Supporting Information [40]). The entire aggregation process takes about 180 s, and no visible nanodroplets are observed around the aggregation after the process is complete. The long aggregation time is due to the difficulty associated with manipulating the nanodroplets, which can be attributed to their high specific gravity (approximately 1.7) and nanoscale size. Furthermore, the results show that the transverse radius of the aggregation is always larger than the longitudinal radius, which may be due to the effect of gravity. However, both the longitudinal and transverse radii, as well as the aggregation area, grow rapidly at first, and then tend to increase gradually, as shown in Figs. 3(b) and 3(c).

The location of the nanodroplet aggregation can be further regulated by adjusting the relative positions of the blood-vessel phantom and the acoustic vortex transducer, as shown in Fig. 4(a) (see also Video S2 in the Supplemental Material [40]). In this study, the blood-vessel phantom

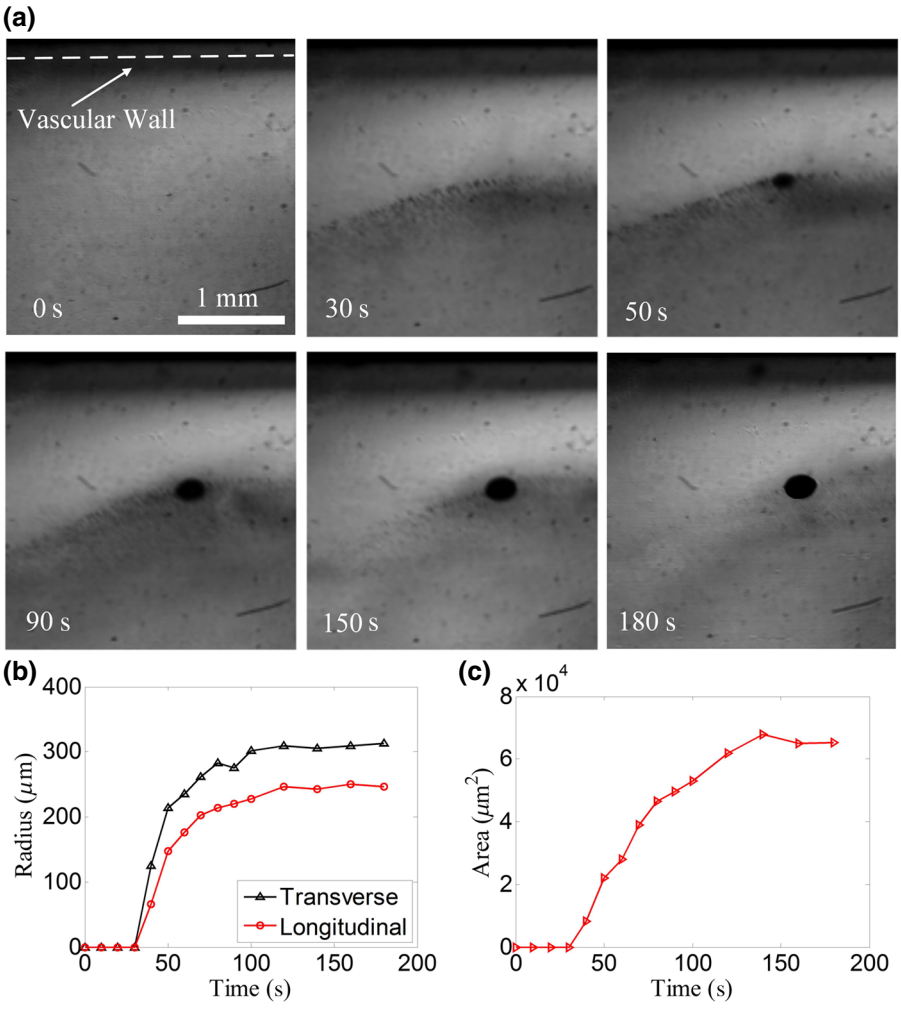

FIG. 3. (a) Microscopic images for the aggregation process of the intravascular dispersed nanodroplets in a blood-vessel phantom. The (b) radius and (c) area of the nanodroplet aggregation as a function of time. The concentration of dispersed nanodroplets is 1.64×10^{10} droplets/ml.

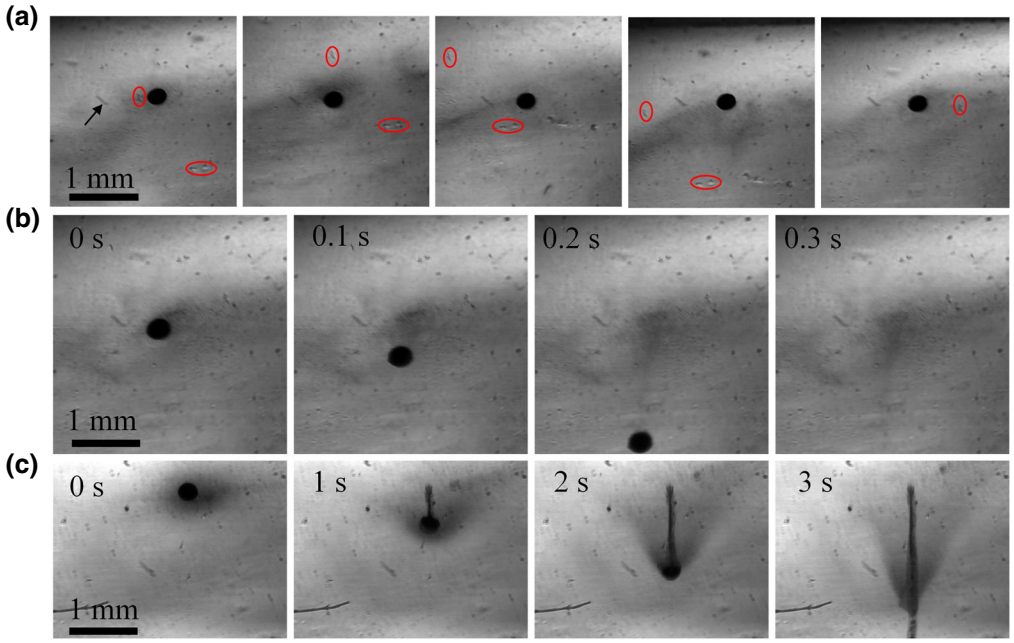

FIG. 4. Regulation and falling process of the nanodroplet aggregation. (a) Regulation of the aggregation location relative to the blood-vessel phantom. The red ellipses in the images indicate the small scratches in the vascular wall, which are generated during the fabrication of the phantom, and can be used as markers to observe the movement of the vessel. The shadow, marked by the black arrow, is caused by dust on the microscope lens, which is difficult to clean completely. Two falling patterns of the nanodroplet aggregation when the power source for the acoustic vortex transducer is switched off: (b) the aggregation drops down rapidly and the shape is preserved; (c) the aggregation drops down slowly and the shape changes.

is manually moved at an approximate speed of 0.25 mm/s by a 3D position controller, while the position of the acoustic vortex transducer is kept fixed. It is worth noting that during the regulation the aggregation has a stable morphology and the dispersed nanodroplets near the regulation route can be captured into it, thus increasing the number of nanodroplets in the aggregation. When the power source for the acoustic vortex transducer is switched off, the nanodroplet aggregation drops down due to the effect of gravity. It is found that the aggregation drops down in two patterns. (1) The nanodroplet aggregation drops down rapidly, and its shape is preserved, as shown in Fig. 4(b). This indicates that the aggregation does not come into contact with the vessel wall during the falling process. (2) The nanodroplet aggregation drops down slowly and changes shape, leaving a portion of nanodroplets on the way down, as shown in Fig. 4(c), which indicates that the aggregation slides along the vessel wall as it falls. The different falling patterns indicate that the nanodroplet aggregation can locate near the vascular center or the vascular wall in the blood-vessel phantom, according to the position of the acoustic vortex focus inside the vascular chamber.

Previous studies have shown that solid particles and gaseous bubbles are aggregated into a cluster at the acoustic vortex center [18,21,26], where the pressures are lower than those in the peripheral region. However, it is hypothesized that in a uniform acoustic vortex, perfluorocarbon nanodroplets are aggregated into a ring at the periphery because of their negative acoustic contrast factor compared to the surrounding water [39]. But this turns out to be contrary to the results obtained in this study. It is inferred that the nonuniform distribution of the acoustic pressure is the fundamental mechanism for the elliptical aggregation of the nanodroplets. In order to verify this hypothesis, the ARFs acting on the microbubbles (mean radius 2.5 μm) and the perfluorocarbon nanodroplets (mean radius 200 nm) are calculated basing on the scanned data of the generated nonuniform focused acoustic vortex. Figure 5(a) shows that, in the nonuniform acoustic vortex, the distribution of the ARFs acting on the microbubbles is similar to the distribution in a uniform acoustic vortex [25]. This indicates that the dispersed microbubbles in the nonuniform acoustic vortex are still aggregated into a cluster located at the vortex center. However, it is observed that the ARFs acting on the nanodroplets are deflected, and seem to converge at a certain point in the nonuniform distribution region of the acoustic pressure, where the nanodroplet aggregation is expected to form, as shown in Figs. 5(b) and 5(c). Additionally, the theoretical value of the distance between the nanodroplet and microbubble aggregations can be obtained by extracting the coordinates of the ARF convergence points in Figs. 5(a)–5(c).

However, due to the limited spatial accuracy of the scanned nonuniform focused acoustic vortex, the vector

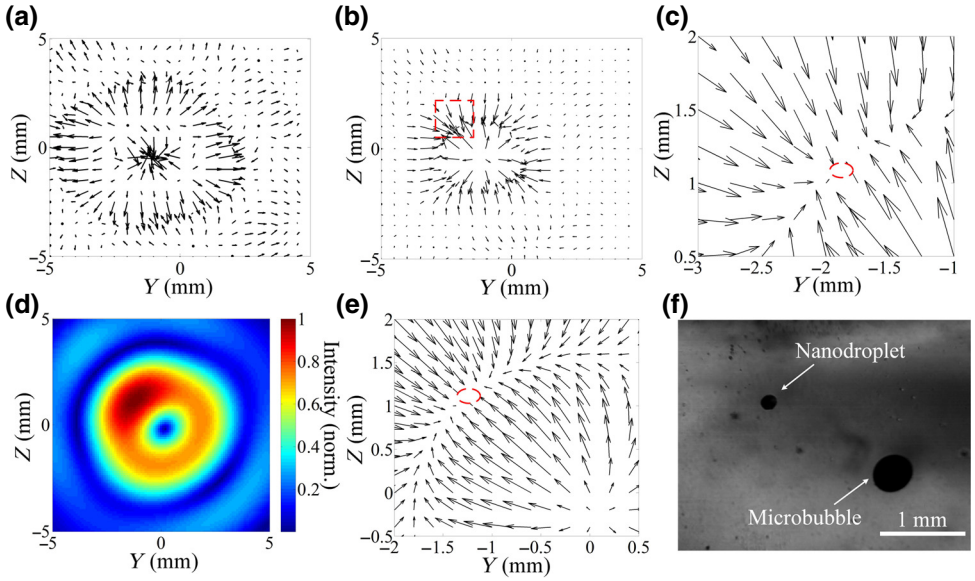

FIG. 5. The ARFs acting on (a) the microbubbles and (b) the nanodroplets in the generated nonuniform focused acoustic vortex. (c) Enlargement of the red box in (b). (d) The normalized pressure distribution in the transverse plane of the focus in the simulated nonuniform focused acoustic vortex. (e) ARFs acting on the nanodroplets in the nonuniform distribution region of the pressures in the simulated acoustic vortex. (f) Photograph of the nanodroplet and microbubble aggregations obtained in the generated nonuniform focused acoustic vortex. The red ellipses in (c) and (e) indicate the predicted location of the nanodroplet aggregation.

distribution of the ARFs acting on the nanodroplets cannot be analyzed more precisely using the scanning data. In order to overcome this issue, we further simulate the nonuniform focused acoustic vortex generated in the study, which shows good consistency, as shown in Fig. 5(d). It is clearly indicated that in the nonuniform distribution region of the acoustic pressure, the ARFs acting on the nanodroplets converge at a certain point, where the dispersed nanodroplets are aggregated, as shown in Fig. 5(e). In order to further validate the above theory, we pump a nanodroplet emulsion containing very few microbubbles (SonoVue, Bracco SpA, Milan, ITA, mean diameter 2.5 μm) into the blood-vessel phantom, and then generate a nonuniform focused acoustic vortex to manipulate both the nanodroplets and the microbubbles simultaneously. Figure 5(f) shows that the dispersed nanodroplets and microbubbles are aggregated in different regions, and the nanodroplet aggregation is located at the upper left in relation to the microbubble aggregation, which shows good consistency with the calculation results of the ARFs. The distance between the nanodroplet and microbubble aggregations obtained in the experiments is further calculated to be 1.62 ± 0.06 mm, which is very close to the theoretical value (1.56 ± 0.1 mm). The small deviation between the theoretical and experimental values of the distance may be due to the low scanning accuracy of the generated nonuniform focused acoustic vortex, which would affect the theoretical prediction of the nanodroplet aggregation position. Based on these results, it can be concluded that the reason why the nanodroplet aggregation appears as an ellipse, rather than as a ring, in this study is attributed to the nonuniform distribution of the acoustic pressure, which makes the ARFs acting on the nanodroplets converge at a certain point.

In perfluorocarbon nanodroplet-assisted ultrasonic diagnosis and therapy, there is a contradictory problem of how to effectively lower the ADV threshold, while maintaining the active size range of the generated microbubbles, which is necessary to ensure the generation of inertial cavitation and the corresponding physical effects [8]. In this study, we further explore the effects of nanodroplet aggregation on the ADV threshold and the initial radius distribution of the generated microbubbles using the same method as that described in Ref. [8]. Figure 6(a) indicates that the ADV threshold of the aggregation is significantly lower than that of the dispersed nanodroplets at the same concentration, and both varied inversely with the initial concentration. The reduction of the ADV threshold after nanodroplet aggregation may be attributed to two aspects. First, the number and concentration of the nanodroplets in the target area increases after aggregation. Second, the nanodroplet aggregation may focus the incoming wave similarly to that of an individual microdroplet, which has been demonstrated to cause the negative pressure in the microdroplet to be amplified several to tens of times, thus reducing the required incoming wave intensity for ADV [41]. Figure 6(b) shows that, although the generated microbubble sizes of the aggregation are slightly larger than those of the dispersed nanodroplets at the same concentration, they are in the same order of magnitude, thus

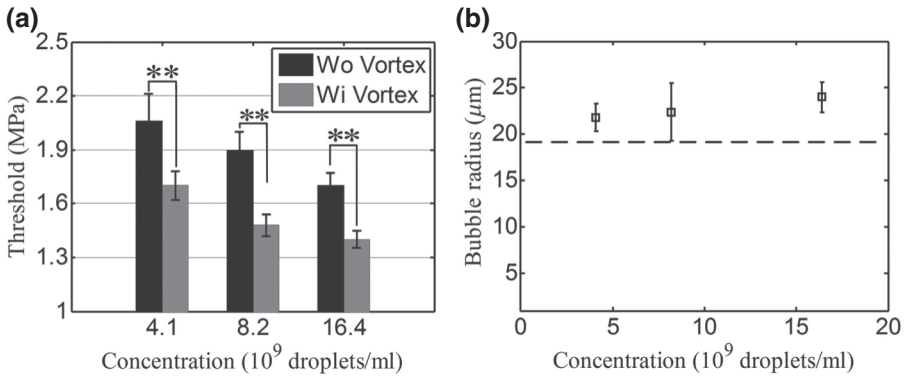

FIG. 6. (a) ADV threshold and (b) initial radius of the generated microbubbles of the nanodroplet aggregations as a function of the concentration. "Wo Vortex" and "Wi Vortex" mean the ADV of nanodroplets without or with the application of the nonuniform acoustic vortex ($^{**}p < 0.01$). The dotted line in (b) indicates the mean vaporized bubble radius of the dispersed nanodroplets with a concentration of 1.64×10^{10} droplets/ml.

ensuring that they can oscillate strongly as a result of an applied acoustic field with further inertial cavitation [42]. The slight increase in the microbubble size may be due to the close proximity of adjacent nanodroplets in the aggregation, which would promote the fusion of microbubbles under the action of the ultrasonic pulse.

IV. CONCLUSION

In conclusion, this study demonstrates that the dispersed perfluorocarbon nanodroplets can be manipulated to form a micron-sized elliptical aggregation via a nonuniform focused acoustic vortex, and the location of the aggregation can be further flexibly regulated. It is shown theoretically and experimentally that the underlying mechanism for the elliptical aggregation is the nonuniform distribution of the acoustic pressure, which causes the ARFs acting on the nanodroplets to converge at a certain point. Furthermore, the findings show that the ADV threshold of the nanodroplets is significantly lowered after aggregation, while a similar size range of the microbubbles generated by dispersed nanodroplets is maintained. It is expected that this study will provide an alternative field of opportunities for drug delivery and imaging using nanodroplets and will also offer a variety of interesting possibilities for the development of future devices or studies.

ACKNOWLEDGMENTS

This work was supported by the National Natural Science Foundation of China (Grant No. 81827801), Project funded by China Postdoctoral Science Foundation (No. 2019M650265), and the National Natural Science Foundation of China (Grants No. 81771854, No. 11874049, and No. 11474229).

[1] V. P. Torchilin, Multifunctional, stimuli-sensitive nanoparticulate systems for drug delivery, Nat. Rev. Drug Discov. **13**, 813 (2014).
[2] S. R. Sirsi and M. A. Borden, State-of-the-art materials for ultrasound-triggered drug delivery, Adv. Drug Deliver. Rev. **72**, 3 (2014).
[3] S. Mura, J. Nicolas, and P. Couvreur, Stimuli-responsive nanocarriers for drug delivery, Nat. Mater. **12**, 991 (2013).
[4] T. D. Martz, D. Bardin, P. S. Sheeran, A. P. Lee, and P. A. Dayton, Microfluidic generation of acoustically active nanodroplets, Small **8**, 1876 (2012).
[5] P. S. Sheeran and P. A. Dayton, Phase-change contrast agents for imaging and therapy, Curr. Pharm. Des. **18**, 2152 (2012).
[6] K. Tachibana, T. Uchida, K. Ogawa, N. Yamashita, K. Tamura, and K. Ogawa, Induction of cell-membrane porosity by ultrasound, Lancet **353**, 1409 (1999).
[7] I. Lentacker, C. I. De, R. Deckers, S. C. D. Smedt, and C. T. W. Moonen, Understanding ultrasound induced sonoporation: Definitions and underlying mechanisms, Adv. Drug Deliv. Rev. **72**, 49 (2014).
[8] S. Guo, A. Shi, S. Xu, X. Du, X. Wang, Y. Zong, A. Bouakaz, and M. Wan, Lowering of acoustic droplet vaporization threshold via aggregation, Appl. Phys. Lett. **111**, 254102 (2017).
[9] Y. Li, C. Lee, R. Chen, Q. Zhou, and K. K. Shung, A feasibility study of *in vivo* applications of single beam acoustic tweezers, Appl. Phys. Lett. **105**, 173701 (2014).
[10] F. Guo, W. Zhou, P. Li, Z. Mao, N. H. Yennawar, J. B. French, and T. J. Huang, Precise manipulation and patterning of protein crystals for macromolecular crystallography using surface acoustic waves, Small **11**, 2710 (2015).
[11] E. H. Brandt, Suspended by sound, Nature **413**, 474 (2001).
[12] D. Foresti, M. Nabavi, M. Klingauf, A. Ferrari, and D. Poulikakos, Acoustophoretic contactless transport and handling of matter in air, Proc. Natl Acad. Sci. U. S. A. **110**, 12549 (2013).
[13] C. R. P. Courtney, B. W. Drinkwater, C. E. M. Demore, S. Cochran, A. Grinenko, and P. D. Wilcox, Dexterous manipulation of microparticles using Bessel-function acoustic pressure fields, Appl. Phys. Lett. **102**, 123508 (2013).
[14] J. R. Wu, Acoustical tweezers, J. Acoust. Soc. Am. **89**, 2140 (1991).
[15] T. Laurell, F. Petersson, and A. Nilsson, Chip integrated strategies for acoustic separation and manipulation of cells and particles, Chem. Soc. Rev. **36**, 492 (2007).
[16] M. Evander and J. Nilsson, Acoustofluidics 20: Applications in acoustic trapping, Lab Chip **12**, 4667 (2012).
[17] A. Marzo, S. A. Seah, B. W. Drinkwater, D. R. Sahoo, B. Long, and S. Subramanian, Holographic acoustic elements

for manipulation of levitated objects, Nat. Commun. **6**, 8661 (2015).
[18] S. T. Kang and C. K. Yeh, Potential-well model in acoustic tweezers, IEEE T. Ultrason. Ferr. **57**, 1451 (2010).
[19] K. V. Sepúlveda, A. O. Santillán, and R. R. Boullosa, Transfer of Angular Momentum to Matter From Acoustical Vortices in Free Space, Phys. Rev. Lett. **100**, 024302 (2008).
[20] A. Anhäuser, R. Wunenburger, and E. Brasselet, Acoustic Rotational Manipulation Using Orbital Angular Momentum Transfer, Phys. Rev. Lett. **109**, 034301 (2012).
[21] D. Baresch, J. L. Thomas, and R. Marchiano, Observation of a Single-Beam Gradient Force Acoustical Trap for Elastic Particles: Acoustical Tweezers, Phys. Rev. Lett. **116**, 024301 (2016).
[22] B. T. Hefner and P. L. Marston, An acoustical helicoidal wave transducer with applications for the alignment of ultrasonic and underwater systems, J. Acoust. Soc. Am. **106**, 3313 (1999).
[23] L. Zhang and P. L. Marston, Angular momentum flux of nonparaxial acoustic vortex beams and torques on axisymmetric objects, Phys. Rev. E **84**, 065601 (2011).
[24] K. D. Skeldon, C. Wilson, M. Edgar, and M. J. Padgett, An acoustic spanner and its associated rotational Doppler shift, New J. Phys. **10**, 013018 (2008).
[25] Z. Hong, J. Zhang, and B. W. Drinkwater, Observation of Orbital Angular Momentum Transfer From Bessel-Shaped Acoustic Vortices to Diphasic Liquid-Microparticle Mixtures, Phys. Rev. Lett. **114**, 214301 (2015).
[26] W. C. Lo, S. T. Kang, and C. K. Yeh, in *Proceedings of the IEEE International Ultrasonics Symposium (IUS)* (2015). https://ieeexplore.ieee.org/document/7329439/
[27] R. Marchiano, F. Coulouvrat, L. Ganjehi, and J. L. Thomas, Numerical investigation of the properties of nonlinear acoustical vortices through weakly heterogeneous media, Phys. Rev. E **77**, 016605 (2008).
[28] X. Fan, Z. Zou, and L. Zhang, Acoustic vortices in inhomogeneous media, Phys. Rev. Res. **1**, 032014 (2019).
[29] Y. J. Ho and C. K. Yeh, Concurrent anti-vascular therapy and chemotherapy in solid tumors using drug-loaded acoustic nanodroplet vaporization, Acta Biomater. **49**, 472 (2017).
[30] Y. Zhou, Application of acoustic droplet vaporization in ultrasound therapy, J. Ther. Ultrasound **3**, 20 (2015).
[31] S. Guo, X. Du, X. Wang, S. Lu, A. Shi, S. Xu, A. Bouakaz, and M. Wan, Reduced clot debris size using standing waves formed via high intensity focused ultrasound, Appl. Phys. Lett. **111**, 123701 (2017).
[32] Y. Qiao, H. Yin, Z. Li, and M. Wan, Cavitation distribution within large phantom vessel and mechanical damage formed on surrounding vessel wall, Ultrason. Sonochem. **20**, 1376 (2013).
[33] S. Guo, X. Guo, X. Wang, D. Zhou, X. Du, M. Han, Y. Zong, and M. Wan, Reduced clot debris size in sonothrombolysis assisted with phase-change nanodroplets, Ultrason. Sonochem. **54**, 183 (2019).
[34] N. Reznik, O. Shpak, E. C. Gelderblom, R. Williams, N. De Jong, M. Versluis, and P. N. Burns, The efficiency and stability of bubble formation by acoustic vaporization of submicron perfluorocarbon droplets, Ultrasonics **53**, 1368 (2013).
[35] M. Lu, M. Wan, F. Xu, X. Wang, and H. Zhong, Focused beam control for ultrasound surgery with spherical-section phased array: Sound field calculation and genetic optimization algorithm, IEEE Trans. Ultrason. Ferroelectr. Freq. Control **52**, 1270 (2005).
[36] M. Lu, X. Wang, M. Wan, Y. Feng, F. Xu, H. Zhong, and J. Tan, Image-guided 256-element phased-array focused ultrasound surgery - system and multifocus pattern control, IEEE Eng. Med. Biol. Mag. **27**, 84 (2008).
[37] T. G. Leighton, A. J. Walton, and M. J. W. Pickworth, Primary Bjerknes forces, Eur. J. Phys. **11**, 47 (1990).
[38] B. Raiton, J. R. Mclaughlan, S. Harput, P. R. Smith, D. M. J. Cowell, and S. Freear, The capture of flowing microbubbles with an ultrasonic tap using acoustic radiation force, Appl. Phys. Lett. **101**, 044102 (2012).
[39] C. S. Hall, G. M. Lanza, J. H. Rose, R. J. Kaufmann, R. W. Fuhrhop, S. H. Handley, K. R. Waters, J. G. Miller, and S. A. Wickline, Experimental determination of phase velocity of perfluorocarbons: Applications to targeted contrast agents, IEEE Trans. Ultrason. Ferroelec. Freq. Control **47**, 75 (2000).
[40] See Supplemental Material at http://link.aps.org/supplemental/10.1103/PhysRevApplied.13.034009 for the videos.
[41] O. Shpak, M. Verweij, H. J. Vos, N. De Jong, D. Lohse, and M. Versluis, Acoustic droplet vaporization is initiated by superharmonic focusing, Proc. Natl Acad. Sci. U. S. A. **111**, 1697 (2014).
[42] K. Yasui, T. Tuziuti, J. Lee, T. Kozuka, A. Towata, and Y. Iida, The range of ambient radius for an active bubble in sonoluminescence and sonochemical reactions, J. Chem. Phys. **128**, 184705 (2008).